A MACRO-DISTINCT ELEMENT MODEL (M-DEM) FOR OUT-OF-PLANE ANALYSIS OF UNREINFORCED MASONRY STRUCTURES

D. Malomo[1], **M.J. DeJong** [2]

[1] McGill University, Department of Civil Engineering, 817 Sherbrooke Street, Montréal, Québec, H3A 0C3, Canada, daniele.malomo@mcgill.ca (corresponding author)
[2] University of California, Berkeley, Department of Civil and Environmental Engineering, 777 Davis Hall, Berkeley, California, 94720, United States. email: dejong@berkeley.edu

ABSTRACT

Despite the vulnerability of unreinforced masonry (URM) structures to out-of-plane (OOP) loading, computational methods that can efficiently simulate OOP failure at the building scale are still limited. Current methods typically rely on simplified static analysis approaches or refined micro-modeling techniques that entail high computational expense, thus limiting their employment to reduced-scale and local problems. With a view to overcome these issues, a novel Finite-Distinct macroelement model which combines the efficiency of simplified modeling strategies with the multifaceted capabilities of discontinuum-based methods, is developed and implemented in the framework of the Distinct Element Method (DEM). Shear and flexural failure modes, either in-plane or out-of-plane, are accounted for by zero-thickness interface spring layers, whose layout is determined *a priori* as a function of the considered masonry bond pattern. Meanwhile, crushing failure is modeled through homogenized Finite Element macro-blocks. The proposed discretization scheme is conceived so that the model can also be used to simulate in-plane damage, for which the model has already been validated. Simplified expressions are proposed for determining equivalent mechanical properties of the interface spring layers, depending on their inclination. Similarly, analytically-based equations are used to significantly reduce the number of springs needed to adequately reproduce the OOP bending response at the joint level. Numerical simulations are compared to previous experimental quasi-static and dynamic tests on both brick and block URM components, characterized by markedly different vertical pressures, aspect ratios, boundary conditions and confinement; both one-way and two-way bending actions are considered. The results indicate that the model can satisfactorily reproduce the measured load-displacement curves in a reasonable timeframe, as well as the experimentally-observed failure mechanisms.

Keywords: out-of-plane; macroelement; Finite-Distinct Element Method; unreinforced masonry; confined masonry

1. INTRODUCTION

The out-of-plane (OOP) failure of unreinforced masonry (URM) assemblies often precludes the exploitation of the global capacity associated with the in-plane (IP) resistance of URM members. Indeed, separation between transversal and longitudinal walls [1,2] and ineffectiveness of façade-diaphragm connections [3,4] might lead to the development of early collapse phenomena. Notwithstanding the possibility of obtaining unconservative predictions, the effects of local OOP failures, as well as the mechanical interaction among elements subjected to IP-OOP combined actions, are typically neglected by most of the presently-available simplified numerical approaches (e.g. [5,6] that are widely used by practitioners for full-scale buildings because of the reduced computational expense. Although promising novel modeling strategies are currently being explored, as further discussed in what follows, the low-cost numerical assessment of OOP-governed responses of URM structures still represents an open challenge.

Equivalent frame simulation of a full-scale shake-table-tested URM building prototype has been proposed [7], in which the nonlinear contribution of OOP-loaded walls was considered by modeling them in the direction of motion, albeit without explicitly accounting for the effect of local failure mechanisms. This initial scheme was recently upgraded to include a newly-developed macroelement formulation [8], and validated against the dynamic response of a series of URM specimens. However, two-way bending OOP failures were not modeled, and a comprehensive validation process is still needed when considering either irregular opening layouts, non-periodic masonry or complex geometries. Indeed, in the latter case, the identification of the effective wall height and the definition of the equivalent frame becomes non-unique and may lead to non-negligible epistemic modeling errors (see e.g. [9,10]). Additional cost-effective modeling approaches for simulating OOP failure of URM structures rely on rigid body kinematics and multi-body dynamics, as those presented in e.g. [11–13], whose arrangement is often based on geometrical considerations and simplified assumptions. Despite the latter are usually supported by post-earthquake damage observations and the good agreement with experimental outcomes found by several authors, the fact that failure mechanisms need to be determined *a priori*, while infinite-compression and zero-

tension models are often employed, makes this approaches not suitable for the modeling of mortared URM structures, IP-OOP cumulative damage and complex mechanisms involving crushing phenomena.

As discussed in D'Altri et al. [14] and Sorrentino et al. [15], to which interested readers are referred for a detailed review of presently-available options for the analysis of URM structures, more complex meso and micro-scale computational procedures have been also applied to the modeling of the OOP response of URM systems. Discontinuum-based techniques, including Discrete Element (e.g. [16,17]) and rigid body ad spring models (RBSM, see e.g. [18,19]), where either rigid or deformable blocks are usually connected through interface spring layers, proved to be capable of adequately reproducing OOP-governed behavior of URM components [20–22] and reduced-scale building specimens [23–25], also simulating explicitly damage propagation. Similarly, in the framework of continuous and homogenized models, including e.g. those based on the Finite Element (FE) numerical procedures, various authors (e.g. [26–28]) have proposed effective solutions of varying levels of detail for simulating the structural behavior of URM systems, and recent applications (e.g. [29–31] have shown that OOP modes and associated failure mechanisms can be satisfactory replicated numerically. However, such refined modeling strategies typically entail a high computational cost, especially in the post-damage range, thus limiting their applicability to the modeling of local and reduced-scale problems [32].

To overcome the abovementioned limitations, hybrid numerical models, consisting of the mixed-use of interface spring layers and deformable macroelements, have been proposed. Yi at al. [33] analyzed the cyclic response of a statically-loaded two-story URM building prototype by introducing nonlinear discontinuities in FE models corresponding to the experimentally-observed failure locations. Analogous approaches were also used by e.g. [34] and [35] for simulating the response of a C-shaped URM assembly tested under incremental OOP shake-table test (idealized by the authors as an assembly of large and irregular rigid and deformable regions respectively), and reasonable results were obtained. However, given that in the applications above the discrete crack layouts were tailored to the damage pattern of specific tests, their general applicability of the model is limited. Pantò et al. [36] proposed a model in which 7-DOF deformable macroelements are connected through transversal interface links to simulate IP and OOP flexural behavior of adjacent macroelements, while additional interface elements account for shear-sliding, compression and torsion modes. Despite the acceptable results obtained in terms of actual versus numerical failure modes, the possibility of capturing local crushing damage (which might be relevant in the case of hollow units and low-compressive strength masonry types, particularly with confinement) and its impact on the overall OOP capacity is not yet considered. Finally, because of the simplified idealization of URM components, the non-negligible influence of masonry texture on the overall IP-OOP response [37,38] cannot presently be taken into consideration.

In this work, to combine the efficiency of simplified approaches with the multifaceted capabilities of interface-based discrete methods, a new Macro-Distinct Element Model (M-DEM) for the analysis of URM structures is presented and validated against a wide range of laboratory tests on both reduced and full-scale brick and block URM prototypes subjected to either one or two-way bending conditions. In the proposed methodology, compressive failure is accounted for within homogenized FE blocks, enabling simulation of local crushing, while flexural and sliding/diagonal shear phenomena are represented through equivalent interface (or contact) springs, automatically generated at contact points among adjacent elements. The novel approach is implemented within the 3DEC Distinct Element Method (DEM)-based commercial software framework [39] and might be of interest to both practitioners and researchers. Further, the explicit time-integration scheme on which the selected computational platform is founded makes this model compatible with large-displacement and collapse analysis.

2. M-DEM IDEALIZATION OF OUT-OF-PLANE-LOADED URM ASSEMBLIES

In the framework of the M-DEM, a given URM panel is idealized as an assembly of six deformable FE macro-blocks, internally discretized with a tetrahedral mesh and connected through zero-thickness nonlinear interface springs. As shown in **Fig. 1**(a), their layout is determined *a priori* through the definition of the average slope (φ) of the lines connecting consecutive head joints along the wall length, i.e. potential failure planes are identified through the masonry texture. The layout varies as a function of the aspect ratio λ_w (calculated as h_w/l_w, i.e. wall height over its length) of the considered URM member (see **Fig. 1**(b)).

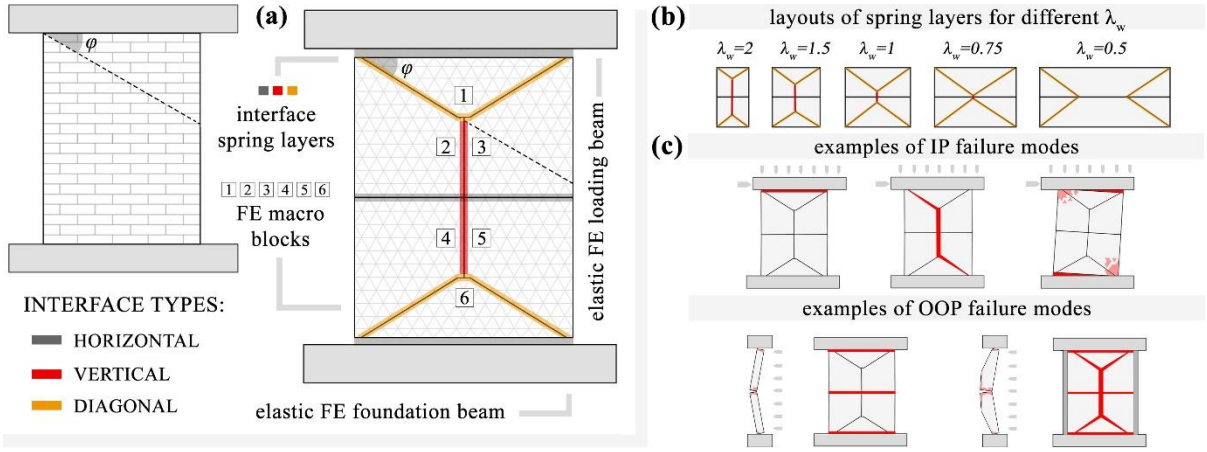

Fig. 1 (a) M-DEM idealization, (b) spring layers layout as a function of the aspect ratio, (c) examples of IP/OOP failures

As previously demonstrated by the authors [40], this modeling strategy is suitable for reproducing the IP failure mechanisms typically observed during experimental tests on URM spandrels [41], isolated wall components [42] and building specimens [43]. Meanwhile, as qualitatively shown in **Fig. 1**(c) and further discussed in what follows, it also enables the possibility of simulating the main OOP collapse modes under both one-way [44] and two-way [45] bending.

Elastic OOP behavior is governed by the deformable FE blocks, to which Young's modulus (E) and shear modulus (G, set to $0.4E$ in this endeavor) of masonry are assigned. Dummy normal and shear stiffnesses are assigned to the spring layers (as further detailed in the next section). The interface springs are characterized by a Mohr-Coulomb failure criterion (no shear softening) with tension cut-off (see **Fig. 2**(a)), thus accounting for system nonlinearity with respect to shear and bending actions. While the friction angle ϕ, cohesion c and tensile strength f_t of horizontal joints (colored in dark grey in **Fig. 1**(a)) are assumed equal to those inferred through triplet and bond wrench tests respectively, equivalent values (i.e. $\bar{\phi}, \bar{c}, \bar{f}_t$) are calculated for the diagonal interfaces (highlighted in orange **Fig. 1**(a))using **Eqs. 1, 2, 3** (where t_j stands for mortar joint thickness). On the other hand, the equivalent shear/tensile strength parameter $\bar{\bar{f}}_t$ (**Eq. 4**) proposed by Beyer [46], evaluated by also considering the resistance provided by interlocking units (with thickness t_u, length l_u and width w_u), is allotted to the vertical joints (red-colored in **Fig. 1**(a)).

$$\bar{\phi} = \frac{\phi\, cos(\varphi) + sin\,(\varphi)}{cos(\varphi) - \phi sin\,(\varphi)} \quad \textbf{(1)} \qquad \bar{c} = \frac{c\, cos\,(\varphi)}{cos(\varphi) - \phi sin\,(\varphi)} \quad \textbf{(2)} \qquad \bar{f}_t = \frac{f_t}{cos\,(\varphi)} \quad \textbf{(3)} \qquad \bar{\bar{f}}_t = \frac{c(t_u + t_j) + (l_u \phi)(\phi + c)/1.5}{2\phi(t_u + t_j)} \quad \textbf{(4)}$$

Similarly to e.g. Pantò et al., [36], local torsional mechanisms are herein accounted for numerically by considering the differential elongation and failure of shear springs along interface joints, whose response is independent from n (i.e. number of uniform mesh subdivisions across the thickness – as extensively discussed in the next section) and governed by G, ϕ, c, as well as calculated acting normal stresses. This simplified modeling strategy has been already validated against small-scale torsion-compression characterization tests performed at the Eucentre laboratory (Pavia, Italy) by Sharma et al. [47] in the work lately presented by Malomo et al. [48], where a good agreement among measured and numerical results (inferred using an interface spring-based micro-modeling technique) were obtained.

To simulate crushing phenomena, a linearized version of the Feenstra-De Borst strain-softening compression model [49] (depicted in **Fig. 2**(b)) was developed by modifying the Mohr-Coulomb plasticity model (MPM) originally proposed by Marti and Cundall [50], and assigned to the FE blocks. By writing the MPM failure envelope equations in terms of principal stresses $\sigma_1, \sigma_2, \sigma_3$ (with $\sigma_1 \leq \sigma_2 = 0 \leq \sigma_3$, see **Eq. 5, 6**) as suggested by Zucchini and Lourenço [51], and applying the maximum-shear-stress criterion of Tresca (i.e. assuming that the internal block friction angle ϕ_b is equal to zero), a simple correlation between a fictitious cohesion within the blocks, c_b, and the uniaxial strength in compression f_c of masonry can be obtained, as shown in **Eq. 7**.

$$(\sigma_1 - \sigma_3)\cos\phi_b = 2c_b - [(\sigma_1 - \sigma_3)(1 + \sin\phi_b)]\tan\phi_b \quad \textbf{(5)} \qquad c_b = \frac{2c\, cos(\phi_b)}{1 - sin(\phi_b)} \quad \textbf{(6)} \qquad f_c = 2c_b = \widehat{f_c} \quad \textbf{(7)}$$

A bilinear stress-strain relationship is assumed up to the elastic strain $\kappa_e = 4f_c/E_m$, followed by linear negative stiffness when the stress exceeds the reference initial yielding point value $f_c/3$, whose adoption is a simplification based on the work of Feenstra and De Borst on the modeling of uniaxial compressive failure of concrete elements [49]. Analogous reference values were also successfully employed by several other researchers for the modeling of brick masonry structures e.g. [52,53].

The ultimate strain $\kappa_u = 3G_c/2hf_c$, where G_c stands for fracture energy in compression and h is the crack bandwidth [54]. In Malomo et al. [40], the adequacy of the abovementioned constitutive laws is shown through comparison with a number of characterization tests on small-scale masonry samples, and demonstrates that the implementation of this fracture energy-based simplified criterion essentially eliminated the mesh-dependency of compression-governed failure predictions, while accounting for the post-peak softening branch typically exhibited by masonry specimens under uniaxial compression. This crushing formulation also enables simulation of local crushing effects during OOP failure in this work, representing a significant advancement with respect to conceptually similar simplified numerical approaches.

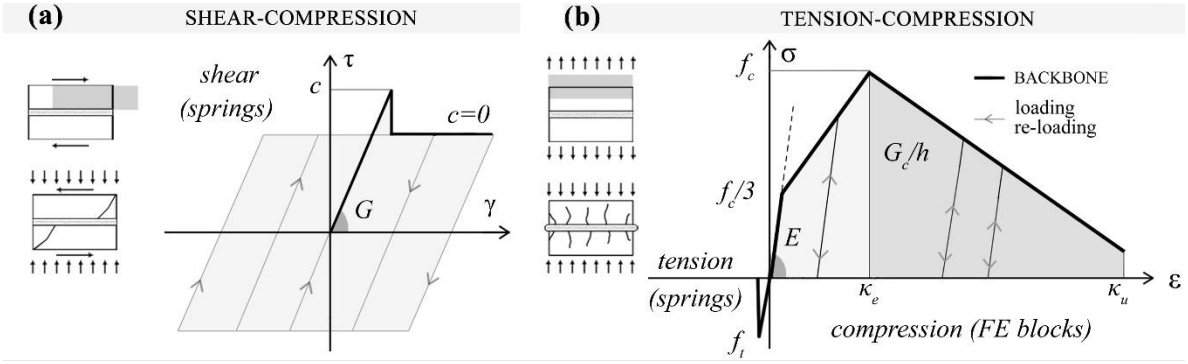

Fig. 2 (a) Shear-compression and (b) tension-compression constitutive laws implemented in the M-DEM model

3. EFFECT OF MESH REFINEMENT ON NUMERICAL PERFORMANCE

In this section, the effect of mesh size on both numerical accuracy and analysis time is investigated. First, the influence of the FE macro-block discretization along the *xz*-plane (see **Fig. 3**) on its elastic response is assessed, considering various degrees of mesh refinements, boundary conditions and aspect ratios. Then, since in the proposed model the characteristics and number of interface springs depends on the extent of *yz*-plane FE mesh subdivisions, a simplified analytical approach is proposed to further reduce the number of interface springs and therefore analysis time, without significantly affecting the quality of results.

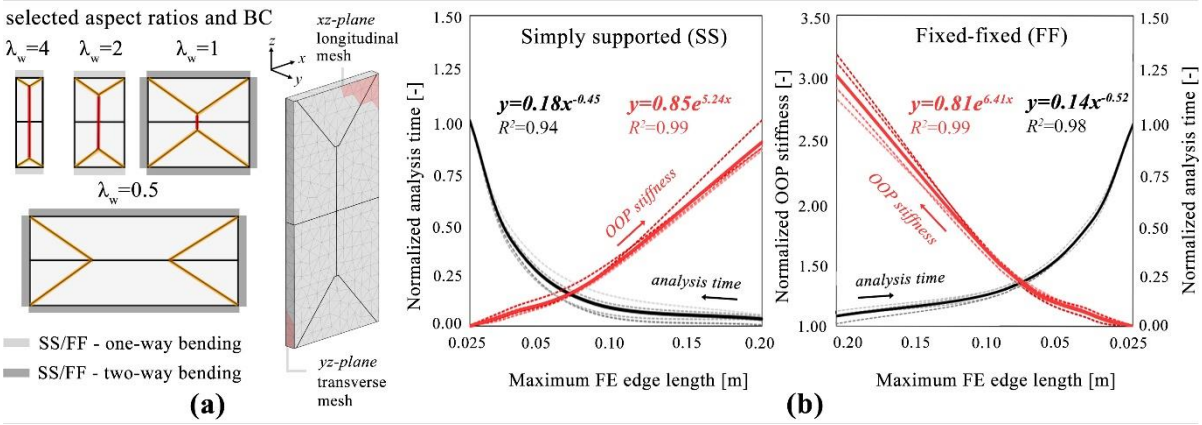

Fig. 3 (a) Selected aspect ratios and boundary conditions, (b) effect of FE mesh size on numerical performance (solid lines represent the best-fit curves, dashed lines represent individual panel results).

When considering IP loading, as shown in [40], the influence of FE mesh size on the M-DEM performance is limited. Contrarily, when subjected to OOP actions, the FE macro-blocks might exhibit different initial mechanical responses depending on the adopted discretization along the *xz*-plane. To address this issue, a sensitivity study is performed that includes the simulation of the elastic behavior of wall members under OOP

actions (no vertical load is applied). Four aspect ratios λ_w (see **Fig. 3**(a)) are considered (representative of both slender (λ_w=4, 2) and squat walls (λ_w=1, 0.5) tested under one and two-way bending respectively), while the wall thickness t_w is 0.15 m for all specimens. Because of the complexity of the boundary conditions (BC) typically imposed to experimentally-tested members, only the extreme cases of simply supported (SS) and fixed-fixed (FF) structures are modeled (only top and bottom edges are constrained for the slender walls subjected to one-way bending, all the edges are constrained for the squat ones under two-way bending). Four *xz*-plane FE mesh dimensions are specified for the macro-blocks, characterized by a maximum element length (EL) of 0.025, 0.05, 0.10 and 0.20. A linearly increasing uniform pressure is applied to the wall until 0.1 mm of OOP mid-height displacement occurs. The assumed Young's modulus is 10000 MPa, and the adopted value of φ is 45°. As shown in **Fig. 3**(b), similar results were obtained for both SS and FF boundary conditions, where the OOP bending stiffness (in red color, normalized with respect to the value obtained with the EL=0.025 model) increases exponentially as a function of EL. As expected, the corresponding computational time (in black color, normalized with respect to that required to perform the EL=0.025 analysis) is instead inversely proportional (best fitting obtained using power-law fitting function). Based on the outcomes of this modeling exercise, a value of EL=0.05 along the *xz*-plane, which represents an acceptable compromise between computational cost and numerical accuracy, is selected and consequently implemented in the M-DEM models employed in the rest of this paper. Analogous values were adopted in [40] for the simulation of IP-loaded isolated URM components and large-scale façades.

In 3DEC, when contact is detected between two adjacent blocks, and after having specified the maximum allowable EL, faces are arbitrarily triangulated to generate subcontacts, located at contact points, where interface springs are subsequently created. As discussed in [55] and qualitatively represented in **Fig. 4**(a), the tributary area of each sub-contact varies, in general, as a function of the disposition of the finite elements. Indeed, if n is the number of uniform mesh subdivisions across the thickness (n = 3 in Fig. 4(a)), and m is the number of finite elements that converge at a given node, a different tributary area A_t (equal to $m/6n$) is assigned to each *yz*-plane spring depending on the automatically-generated mesh pattern. This means that the distribution of interface properties across the whole contact area A (see **Fig. 4**(b)) is generally not uniform, and inner and outer springs have different material properties, because both spring stiffness and calculated peak tensile force are directly proportional to A. This variability has no influence on translational degrees of freedom at the interface, since the springs work in parallel. However, as further discussed in what follows, the impact on the rotational degrees of freedom might be relevant, particularly for low n values.

For OOP response, numerical studies e.g. [56,57] have confirmed that the number of springs across the wall thickness is important, and the use of a very limited number of interface springs may lead to a significant overestimation of the OOP capacity of rocking components, resulting in unconservative predictions. This effect is well-epitomized in **Fig. 4**(c), which shows the 2D response of a single rigid prismatic block (2 m-high and 0.5 m-wide) resting on a deformable interface, and subjected to lateral top loading. Various values of n (3,10, 20, 100), are considered. Results were normalized by the results for n = 100, which represents a nearly continuous solution. Increasing n increases accuracy, but could entail a prohibitive computational expense (**Fig. 3**(a)).

To balance these competing objectives, a simple procedure is desired to adequately reproduce the smooth curve for n = 100 in Fig. 4(c), while conveniently using a reduced number of n subdivisions. The procedure should also account for the possibility of a non-uniform distribution of inner and outer spring properties. Six parameters can be modified to achieve this goal, namely the inner and outer spring spacing (t_i, t_o), the inner and outer layer Youngs's moduli (E_i, E_o) and the inner and outer layer tensile strengths (f_{ti}, f_{to}). Alternatively, the ratio the inner to outer layer value for each parameter, defined as r_t, r_E, r_{ft} respectively, can be adjusted. By varying these ratios, a large range of responses can be obtained. For example, the simulations in Fig. 4(c) assume $r_t = r_E = r_{ft} = 1$. Assuming again that n = 3, E_o = 10000 MPa and f_{to} = 0.6 MPa, but varying one of these ratios (from 0.1 to 4) while leaving the other ratios equal to one, results in the range of responses in grey in Fig. 4(d). Instead, an optimization procedure for defining these parameters is desired. Since the number of independent variables is limited, as further discussed below, a constrained error minimization problem needs to be solved to infer optimal values of E_i, f_{ti}, E_o, f_{to}, t_i, t_o.

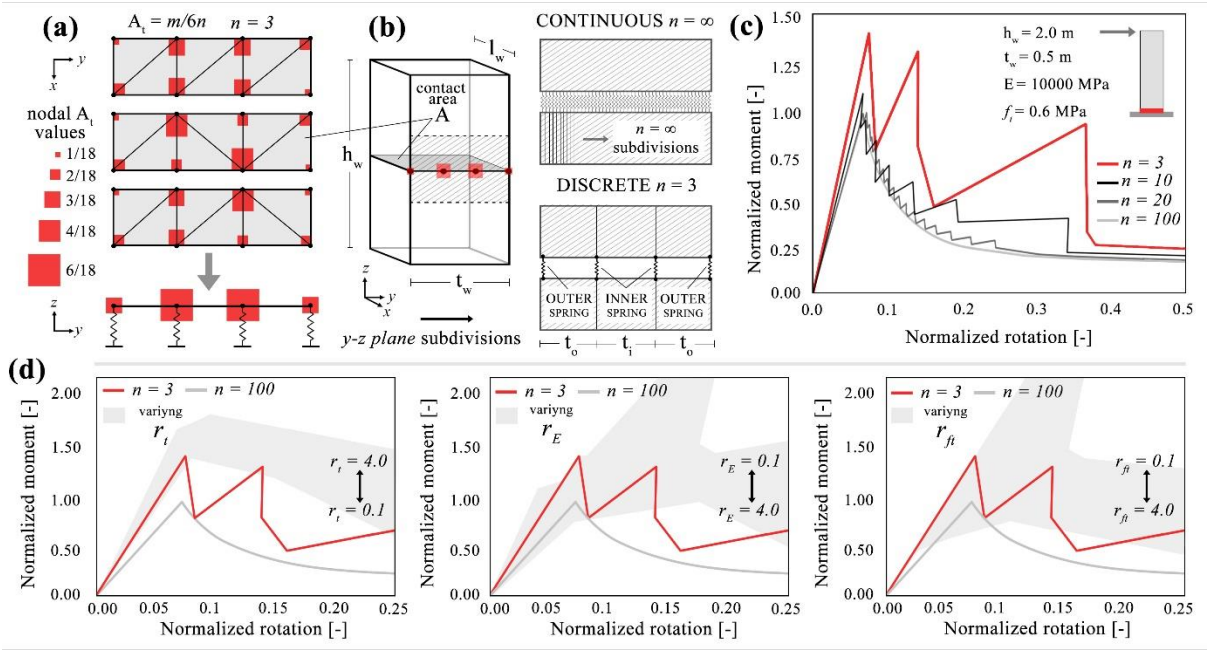

Fig. 4 (a) Nodal A_t values for n = 3, (b) continuous vs. discrete spring system, (c) overturning responses of a free-standing column model with varying n and (d) effect of varying r_t, r_E, and r_{ft} on numerical predictions

The procedure proposed here initially aims to reproduce exactly the initial bending stiffness and peak strength (referred to as maximum moment in this section). Taking as a reference the discrete (with r_t, r_E, $r_{ft}<1$, $n<\infty$, subscript $_D$) and continuous (with r_t, r_E, $r_{ft}=1$, $n=\infty$, subscript $_C$) symmetric systems of **Fig. 4**(b) and considering an applied clockwise small rotation around their centroidal axis, the corresponding bending (or rotational) stiffnesses of the discrete (k_D) and the continuous (k_C) can be computed according to **Eqs. 8** and **9** respectively (with $r_{Ai} = t_o l_w(1+r_t)/(2A)$ and $r_{Ao} = t_o l_w/A$ representing the tributary areas of inner and outer springs normalized with respect to A). **Eq. (8)** is derived by summing up the mechanical contribution of each spring separately (assuming normal stiffnesses of inner and outer springs of the discrete system equal to $k_{iD}=r_{Ao}E_iA/t_j$, $k_{oD}=r_{Ai}E_oA/t_j$, which correspond to those of the continuous one, k_{iC}, k_{oC}, for $r_t = 1$) and imposing equilibrium conditions with respect to the center of stiffness (equal to $t_w/2$ in the initial configuration).

$$k_D = \delta_D\left(\frac{r_{Ao}}{2} + r_{Ai}\Delta_D\right), \quad with \;\; \delta_D = \frac{E_o t_w{}^3 l_w}{t_j}, \;\; \Delta_D = \frac{r_t{}^2(n-2)[n^2 r_E + (3-4r_E)n + 6(r_E-1)]}{12(nr_t - 2r_t + 2)^2} \tag{8}$$

$$k_C = \gamma_C \Gamma_C, \quad with \;\; \gamma_C = \frac{E t_w{}^3 l_w}{t_j}, \;\; \Gamma_C = \frac{(n-1)(n-2)+3n}{12n^2} \tag{9}$$

An analogous approach can be followed for calculating the maximum moments M_D and M_C, as well as the associated small rotations θ_D and θ_C, as summarized in **Eqs. 10** and **11** (note that for diagonal and vertical joints, the tensile strength is modified to $f_t = \bar{f}_t$ and $f_t = \bar{\bar{f}}_t$ respectively). In **Fig. 5**(a), the proposed expressions, equivalent for $r_t = r_E = 1$, are validated against numerical results ($M_{D,\,3DEC}$, obtained using the free-standing column model described above) for various n values, showing adequate agreement.

$$M_D = k_D\theta_D = \delta_D \Delta_D \theta_D, \quad with \;\; \theta_D = \frac{2f_{to}t_j}{E_o t_w} \tag{10}$$

$$M_C = \left(\lim_{n\to\infty} k_C\right)\theta_C = \gamma_C\left(\lim_{n\to\infty}\Gamma_C\right)\theta_C, \quad with \;\; \theta_C = \frac{2f_t t_j}{E_o t_w} \tag{11}$$

By equating k_C to k_D and M_C to M_D, and solving for E_o and f_{to} respectively, the equations above can be rewritten as **Eq. 12, 13**, where the values of E_i and f_{ti} are expressed as a function of r_E, r_{ft}.

$$E_o = \frac{E}{6(r_{Ao} + 2r_{Ai}\Delta_D)}, \quad E_i = r_E E_o \tag{12}$$

$$f_{to} = \frac{f_t}{12(r_{Ao} + r_{Ai}\Delta_D)}, \quad f_{ti} = r_{ft} f_{to} \tag{13}$$

As depicted in **Fig. 5**(a), when using the values inferred with **Eqs. 12** and **13**, the calibrated analytically-derived moment of the discrete system ($M_{D,\,CAL}$) perfectly matches that of its continuous counterpart, for any value of n. **Fig. 5**(b), demonstrates that the reduced-n (in this case n=3) implementing this procedure for the previously

described free-standing column model (for n = 3), both the initial bending stiffness and the maximum moment of the continuous system are reproduced accurately numerically, albeit still noticeably overestimating the dissipated energy. However, according to the constitutive interface spring model employed in this work (see **Fig. 2**), the same Young's modulus and tensile strength parameters for the inner and outer layers must be defined to simultaneously represent uniaxial tension and IP and OOP response; these responses are thus unavoidably coupled, making the equation system above intrinsically indeterminate. To obtain optimal parameters, an error minimization problem is proposed (see **Fig. 5**(c)). Depending on the modeling goals (e.g. IP/OOP-governed behavior), and after having set appropriate constraints and tolerances, an iterative solver (the evolutionary algorithm proposed by [58] was herein employed) is used to compute suitable values of the ratios r_t, r_E, r_{ft} (leading to the definition of E_i, f_{ti}, E_o, f_{to}, t_i, t_o) that keep the error objective functions within acceptable limits. The error objective functions are herein defined as the percentage difference among discrete and continuous quantities.

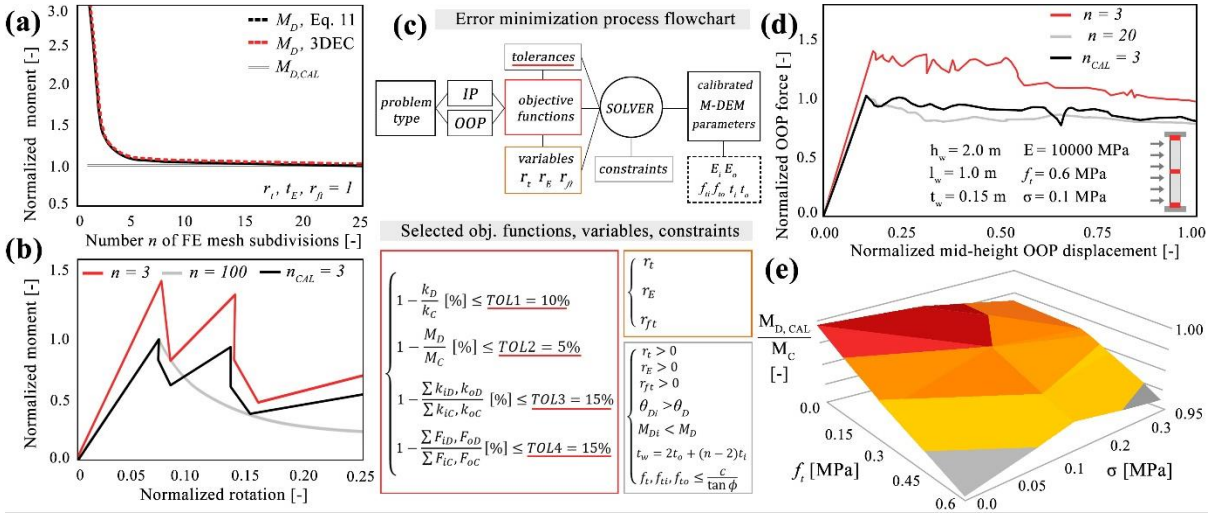

Fig. 5 (a) Analytical validation of Eq. 10, (b) discrete free-standing column models vs. continuous counterpart, (c) error minimization flowchart, (d) discrete OOP-loaded wall models vs. continuous counterpart and (e) associated ratios

Since the main goal of this work is to validate the M-DEM model under OOP loading, the minimization problem has been herein structured to reduce the error related to the simulation of OOP bending-dominated responses. Thus, the error objective functions in the red box in **Fig. 5**(c) have been selected, where F_{iD}, F_{oD}, F_{iC}, F_{oC}, stand for the maximum tensile resisting forces of inner and outer springs of discrete and continuous systems respectively, which also governs the IP bending peak strength. The light gray box in **Fig. 5**(c) shows the constraints, where M_{Di} are the subsequent peaks in resisting moment (after the initial peak), and θ_{Di} are the rotations corresponding to these peaks. These peaks are generated by the response of the inner springs after the failure of the outer one, and can be easily obtained by manipulating **Eqs. 10** and **11**.

The proposed optimization approach was validated against numerical results, this time considering the same M-DEM model presented for the previous mesh sensitivity study (assuming EL = 0.05 m, λ_w = 2 and simply supported conditions), again subjected to an increasing monotonic OOP pressure. Two discretization (n = 3 or n = 20) were considered . The optimization procedure outlined in **Fig. 5**(c) was used to define the parameters for the n_{CAL} = 3 model, while no optimization was employed for the n = 3 and n = 20 models. Note that the n = 20 model adequately matches the continuous solution (see **Fig. 4**(c)) without the need for optimization. **Fig. 5**(d) shows that the n_{CAL} = 3 model satisfactorily reproduces the OOP response predicted by its continuous (i.e. n = 20) counterpart for a specific set of assumed wall material properties (E = 10000 MPa, f_t = 0.6 MPa) and overburden stress (σ = 0.1 MPa). The optimized parameters for this solution are: E_o=6838 MPa, E_i=13936 MPa, t_o=0.059 m, t_i=0.032 m, f_{to} = 00.49 MPa and f_{ti} = 0.81 MPa.

To validate the procedure for a larger range of scenarios, the error in peak moment ($M_{D,CAL}$ / M_C) was quantified for a range of tensile strengths f_t (0.0, 0.3, 0.6 MPa) and vertical loads σ (0.0, 0.1, 0.3 MPa). **Fig. 5**(e) shows that the error ranged from 0.3 to 4.8% across the entire range of simulations, while reducing the average analysis time by approximately 230%. Note that in this modeling exercise, an attempt was made to use tolerance values (*TOL 1-4*) comparable with the scatter typically associated with experimentally-derived masonry parameters (which often results in relatively large coefficients of variation, see e.g. [59]).

4. VALIDATION WITH OUT-OF-PLANE TESTS ON UNREINFORCED MASONRY WALLS

To validate the M-DEM model at the component scale, the outcomes of a number of experimental tests on OOP-loaded URM walls, subjected to either one-way or two-way bending, are compared in this section with numerical predictions. To assess the model capabilities with respect to multiple failure modes, both quasi-static and dynamic responses of clay brick and concrete block panels, characterized by significantly different geometrical and mechanical characteristics, are considered. Regarding FE mesh discretization, analogous assumptions to that of the models of the previous section (whose results are reported in **Fig. 5**(e) are adopted. Similarly, the error minimization algorithm described in **Fig. 5**(c) was employed.

4.1 OUT-OF-PLANE ONE-WAY BENDING TESTS

Eight different full-scale one-way bending tests were simulated. The main test dimensions are summarized in **Table 1** (where λ_s is the slenderness ratio, calculated as h_w/t_w). For clarity, the nomenclature used by the researchers who conducted the original experiments is adopted. The first set of tests considered are those tested in 1971 by Yokel et al. [60], and include solid clay brick walls (i.e. specimens 4-3, 6-3 and 6-7, 1.25 m wide, 2.44 m high, 0.09 m thick) and concrete block walls (i.e. specimen 3-3, 1.21x2.44x0.19 m), with a running-bond pattern, subjected to incremental quasi-static OOP monotonic pressure (imposed with an inflated airbag) until failure. The brick and block masonries are characterized by markedly different f_t values (**Table 1**); this is particularly evident for specimens 3-3 and 6-7, which were both built using high tensile strength mortar. Similarly, the compressive strength f_c of the concrete block wall was 3-4 times lower than the strength of the brick walls. Relatively high vertical top loads (3.86, 5.41, 11.20 and 0.47 MPa, assigned to walls 4-3, 6-3, 6-7 and 3-3 respectively) were imposed through a steel beam, resulting in a crushing-dominated response.

The second set of tests involved double-leaf (with header bricks located at every fourth course) clay brick walls (specimens D1-A and D2-A), tested at the University of Auckland (New Zealand) by Derakhshan in 2013 [61]. The walls were tested under post-cracked conditions (for this reason, $f_t = c = 0$ in **Table 1**). An incremental quasi-static monotonic pressure (plus an unloading cycle for D1-A) was applied in the OOP direction by airbags, while no vertical load was considered. Finally, the third set of tests are dynamic post-cracked OOP tests of two clay brick running-bond URM walls (specimen S10 with no vertical load, and S10ov with a vertical load of 0.075 MPa) tested at the University of Adelaide by Doherty et al. in 2002 [62]. These are release tests, which involved displacing the wall at mid-height close to the point of instability and then releasing it from that position; the wall underwent damped free vibrations until the initial vertical position was reached. Zero damping was implemented in the S10 and S10ov models. Based on the actual experimental setups, partial fixity (bottom) – pinned (top) boundary conditions were imposed for all the selected prototypes.

Table 1 One-way bending walls dimensions and measured/equivalent material properties

Wall	λ_w	λ_s	t_o	t_i	E	E_o	E_i	f_c	f_t	$\bar{f}_t$	$\bar{\bar{f}}_t$	f_{to}	f_{ti}	c	$\bar{c}$	φ	ϕ	$\bar{\phi}$	G_c[1]
ID	[-]		[m]		[MPa]														[N/mm]
3-3	2.0	12.6	0.068	0.054	6206	4244	10511	11.38	0.17	0.24	0.47	0.14	0.26	0.10	0.92	44.3	30	74.41	19.43
4-3	2.0	26.4	0.032	0.026	20685	13768	32091	50.47	0.24	0.34	0.81	0.19	0.33	0.13	0.59	29.3	30	59.41	27.53
6-3	2.0	26.4	0.032	0.026	20685	13768	32091	50.47	1.52	2.15	2.48	1.25	2.11	0.79	2.43	29.3	30	59.41	27.53
6-7	2.0	26.4	0.032	0.026	20685	13768	32091	50.47	1.52	2.15	2.48	1.25	2.11	0.79	2.43	29.3	30	59.41	27.53
D1-A	3.6	17.8	0.084	0.062	1769	1105	2962	6.91	0.00	0.00	0.48	0.00	0.00	0.00	0.00	30.8	30	60.93	17.80
D2-A	3.0	15.2	0.086	0.058	1407	962	2411	5.41	0.00	0.00	0.48	0.00	0.00	0.00	0.00	30.8	30	60.93	17.22
S10	1.6	30	0.019	0.013	9800	5897	16699	26.7	0.00	0.00	0.67	0.00	0.00	0.00	0.00	20.5	30	50.64	23.91
S10ov	1.6	30	0.019	0.013	9800	5897	16699	26.7	0.00	0.00	0.67	0.00	0.00	0.00	0.00	20.5	30	50.64	23.91

[1] Computed as $G_c = 15 + 0.43f_c - 0.036f_c^2$, according to [54]

Experimental outcomes and numerical counterparts are compared in **Fig. 6** in terms of OOP force-displacement curves. Three main quantities are monitored, namely OOP initial bending stiffness, maximum force (i.e. the product between the applied pressure and the airbag-loaded surface) and ultimate displacement capacity at mid-height. The differences between the test and modeling results are expressed though the ratios R_k, R_F, R_d respectively, where predicted values are normalized with respect to the actual ones (i.e. when $R>1$, test values are overestimated). As shown in **Fig. 6**(a) and **Fig. 6**(b), the models adequately reproduced the OOP response of the selected specimens (i.e. the R values are generally close to unity), under either quasi-static or dynamic actions respectively.

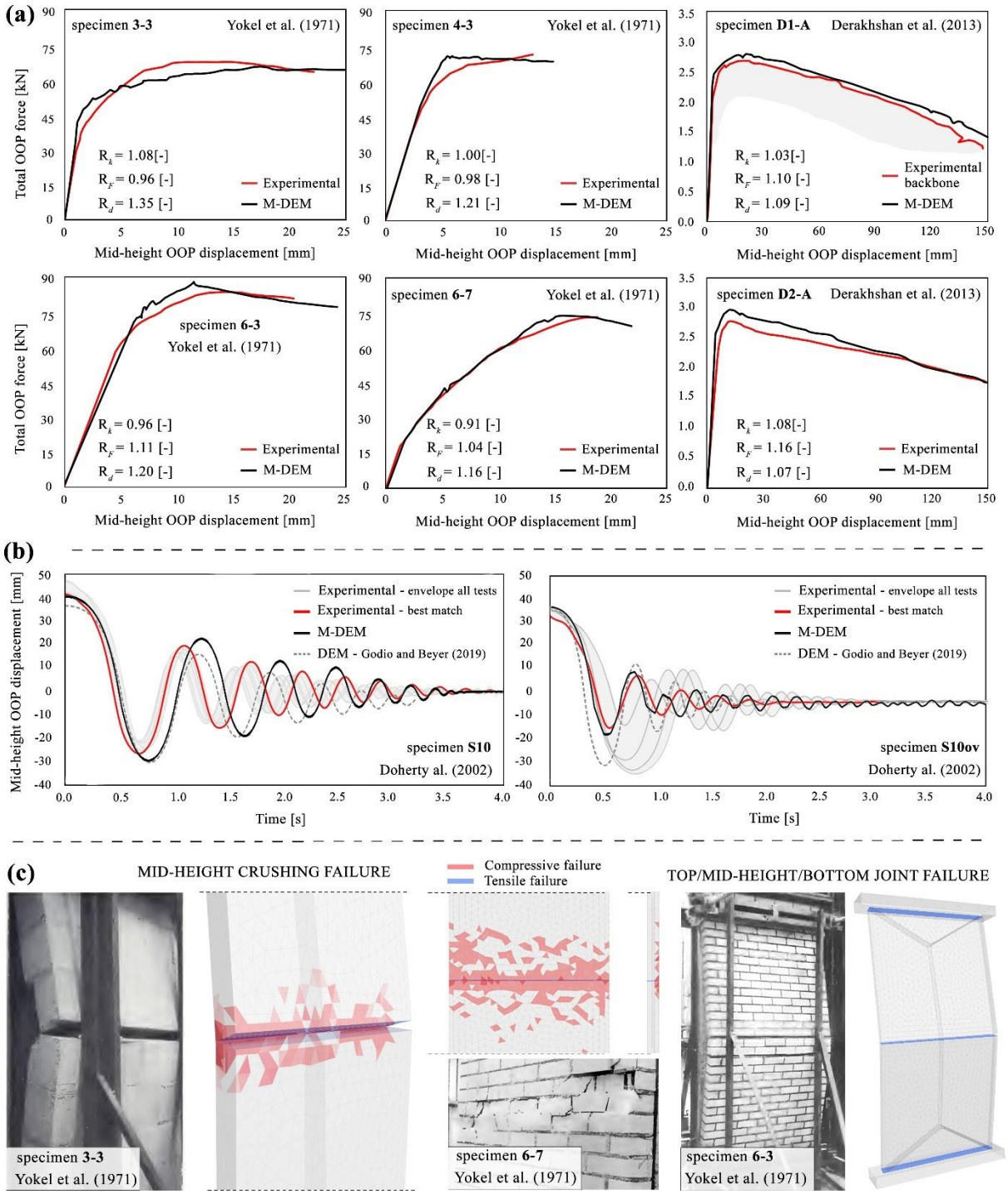

Fig. 6 One-way bending walls: experimental vs. numerical (a) OOP force-displacement curves under quasi-static loads, S10 and S10ov mid-height displacement time histories (c), (b) selected failure modes

In the case of the specimens 3-3 and 6-7, the local crushing failure modes were adequately represented by the model (see **Fig. 6**(c)), although the ultimate displacement capacities were noticeably overestimated. Better agreement for ultimate displacement was found for walls 4-3, 6-3, D1-A and D2-A, whose behavior was governed by mortar joint failure. For the release tests, the results obtained by [20] using a DEM micro model are also included. For S10, the progressive decay of the mid-height OOP displacement was satisfactorily simulated, although the M-DEM model produced a slightly out-of-phase response. For specimen S10ov, the effect of the applied top load was accounted for numerically, also with enhanced accuracy with respect to the DEM outcomes.

4.2 OUT-OF-PLANE TWO-WAY BENDING TESTS

To validate the M-DEM model for OOP two-way bending actions, four different running-bond URM tests were simulated (geometrical and mechanical properties are reported in **Table 2**). All test specimens were simply-supported along their four edges and subjected to incremental quasi-static airbag pressure (with negligible vertical load).

Table 2 Two-way bending walls dimensions and measured/equivalent material properties

Wall	λ_w	λ_s	t_o	t_i	E	E_o	E_i	f_c	f_t	$\bar{f}_t$	$\bar{\bar{f}}_t$	f_{to}	f_{ti}	c	$\bar{c}$	φ	ϕ	$\bar{\phi}$	G_c[1]
ID	[-]		[m]		[MPa]														[N/mm]
8,12	1.5	22.5	0.019	0.014	15000	6765	3401	6	0.12	0.17	0.82	0.09	0.18	0.22	0.38	33.1	30	65.75	17.45
WI	0.8	18.7	0.063	0.023	10000	5921	3201	20	0.32	0.45	1.02	0.23	0.54	0.40	1.59	44.2	30	74.11	22.16
WII	0.6	18.7	0.063	0.023	10000	4781	2134	20	0.32	0.45	1.02	0.23	0.54	0.40	1.59	44.2	30	74.11	22.16

[1] Computed as $G_c = 15 + 0.43f_c - 0.036f_c^2$, according to [54]

The first two panels are identical reduced-scale clay brick prototypes (specimens 8 and 12, 0.79 x 1.19 x 0.053 m) tested at the University of Edinburgh by [63]. Both specimens exhibited similar failure modes, characterized by an hourglass-shaped crack pattern, where mid-height central bricks and those in contact with the fixed external frame also failed in compression. However, the scatter in terms of recorded peak strength capacity is significant, given that the maximum OOP force inferred for wall 12 (whose complete force-displacement curve is not available) is approximately 25% higher than that of wall 8 (see **Fig.7**(a)). The remaining two specimens are concrete block URM panels (specimen WI, 3.4x2.8x0.15 m, and specimen WII, 5.0x2.8x0.15 m) tested at McMaster University by [64]. In this case, mortar joint failure was predominant, although minor damage due to compressive stress localizations was observed at mid-height. During the tests, cracks extended from the center of the panel towards the corners, following the layout of the bond pattern, as depicted in **Fig.7**(c, d).

The OOP response of wall 8/12 predicted by the M-DEM model is in good agreement with the experimental results, for both force-displacement curves and failure modes, particularly in light of the variability between the two identical experimental tests. The numerically-inferred peak OOP force is closer to the wall 12 result (the *R* ratios were computed taking wall 12 as the reference) and agrees well with the prediction by [65] who employed a FEM-based interface meso-model. Of interest is also the similarities in terms of initial bending stiffness and post-peak softening branch. The OOP resistance obtained using the damaging block model recently developed by [22] is slightly lower, yet larger than that of wall 8 so within the experimental variability. When comparing the associated displacement profile at the onset of cracking (corresponding to an OOP displacement of circa 0.35 mm, see **Fig.7**(b)), both the FEM method [22] and the M-DEM model produce deformed shapes similar to the experimental result. The modeling outcomes for the concrete block walls were satisfactory as well (see **Fig.7(**c, d)), with the M-DEM model adequately approximating the experimental force-displacement envelopes and the ultimate displacement capacities. *R* ratios close to the unity were obtained in most of the cases. Although the actual extent of the mid-height masonry crushing has been slightly overestimated numerically, acceptable agreement was found in terms of damage pattern.

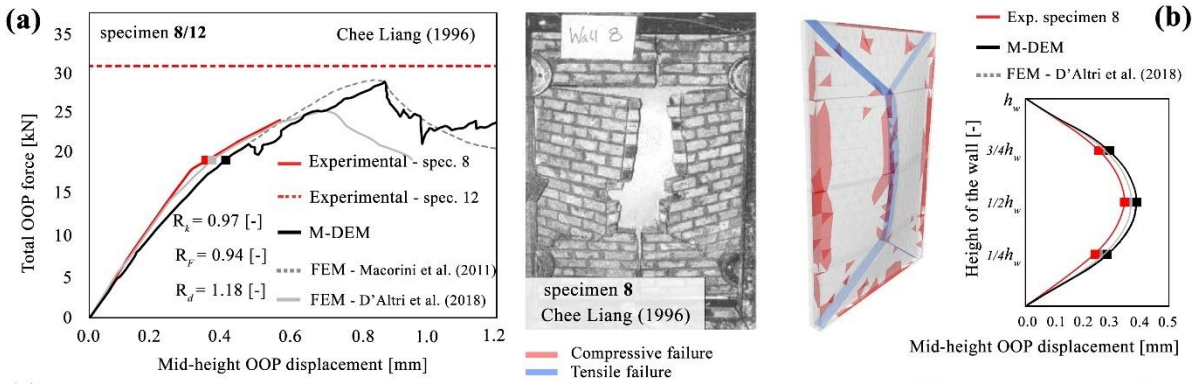

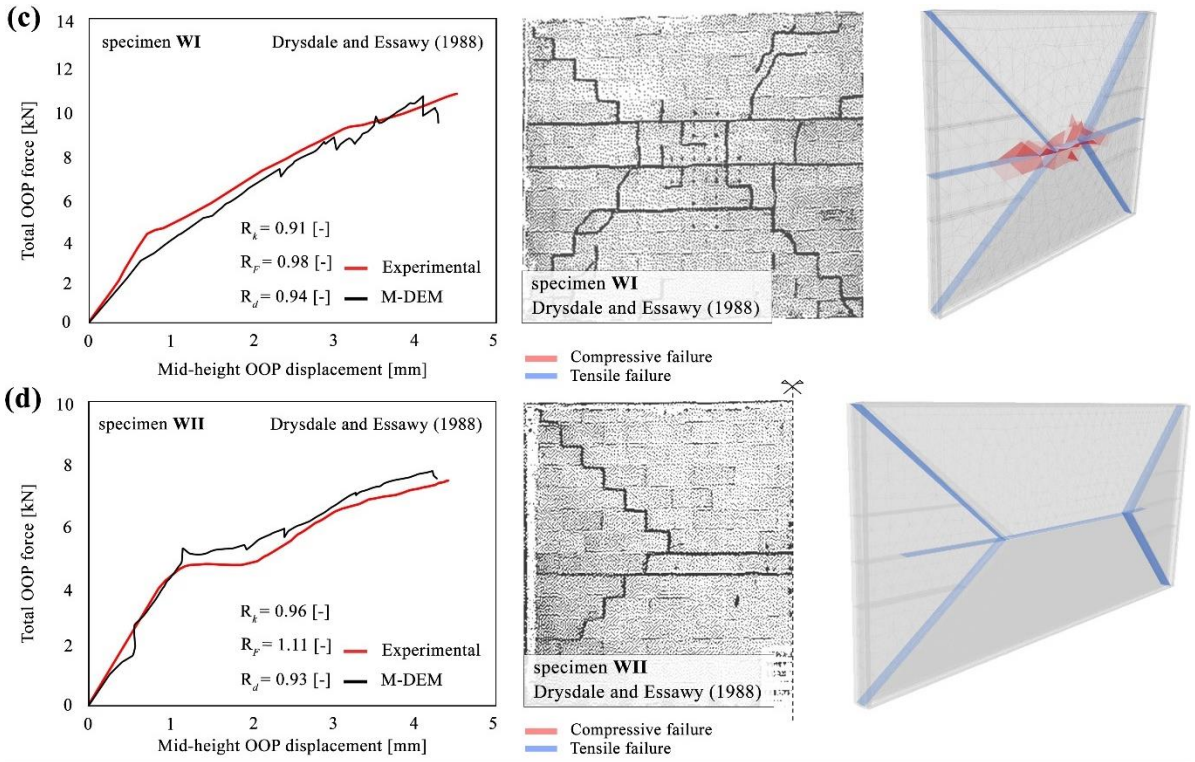

Fig. 7 Two-way bending walls: experimental vs. numerical (a) OOP force-displacement curves, failure modes and (b) displacement profiles for specimens 8/12 [63], OOP force-displacement curves and failure modes for specimens WI (c) and WII (d), [64].

5. EXTENSION TO THE TWO-WAY BENDING BEHAVIOR OF CONFINED MASONRY

Given the positive results obtained in the case of standard URM walls under either one or two-way bending actions, the proposed approach was used to simulate the OOP biaxial monotonic response of confined running-bond masonry wall components (again, no vertical load was considered). Two quasi-static airbag tests conducted by [66,67] at the Autonomous University of Yucatán were modeled using the M-DEM model. Wall specimen E1 (3.6x1.76x0.15 m) featured reinforced concrete (RC) confining elements with a cross-section of 0.15 x 0.15 m; the reinforcement consisted of four 9.5 mm diameter longitudinal steel bars, with 8.3 mm diameter stirrups spaced uniformly every 0.20 m. Wall specimen E4 (2.8x2.7x0.15 m) had the same reinforcement layout but the cross-section measured 0.15 x 0.20 m. Because of the relatively high bending stiffness of the RC members, and since they suffered negligible damage during the tests, a linear elastic isotropic material was assigned to the corresponding numerical elements, with Young's modulus of 10000 MPa [67]. To simulate the frame-wall interaction, a Mohr-Coulomb criterion with tension cut-off was allotted to the frame-wall interface springs. For the masonry elements, the same assumptions made in the previous sections were adopted; the employed material properties are summarized in **Table 3**.

Table 3 Confined masonry walls dimensions and measured/equivalent material properties

Wall	λ_w	λ_s	t_o	t_i	E	E_o	E_i	f_c	f_t	$\bar{f}_t$	$\bar{\bar{f}}_t$	f_{to}	f_{ti}	c	$\bar{c}$	φ	ϕ	$\bar{\phi}$	G_c[1]
ID	[-]		[m]		[MPa]														[N/mm]
E1	0.49	11.73	0.056	0.038	10000	6479	15364	15	0.14	0.2	0.91	0.13	0.32	0.39	0.83	42.3	30	60.11	20.64
E4	0.96	18.67	0.056	0.038	10000	6479	15364	15	0.14	0.2	0.91	0.13	0.32	0.39	0.83	42.3	30	60.11	20.64

[1] Computed as $G_c = 15 + 0.43f_c - 0.036f_c^2$, according to [54]

An adequate agreement was found in terms of force-displacement curves, as shown in **Fig. 8**. The M-DEM failure modes predicted for both E1 (**Fig. 8**(a)) and E4 (**Fig. 8**(b)) walls are also comparable with the experimental counterparts. Both of the specimens exhibited diagonal cracks from the center of the wall to the wall corners. However, the extent of crushing damage in the M-DEM model started to increase significantly after the strength peak, which was not been observed experimentally; only minor cracks due to compressive failure were detected in the experiments. It is also worth noting that in the case of E4, the M-DEM model was capable of reproducing

the uplift of the RC frame due to the interaction with the adjacent wall (see **Fig. 8**(a), lower right side). Note that the vertical displacement was not monitored in the experiment for E1, so it could not be compared.

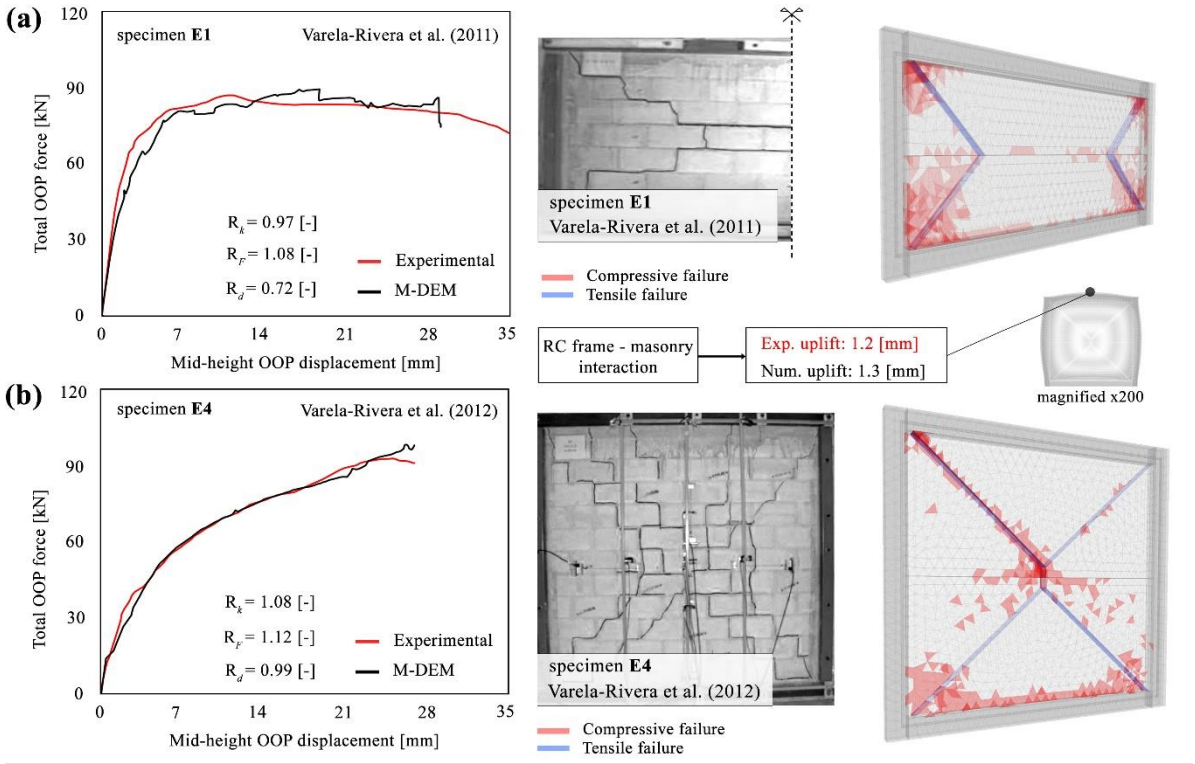

Fig. 8 Confined masonry walls under two-way bending: experimental vs. numerical OOP force-displacement curves and failure modes for E1 [66] and E4 [67] specimens

6. CONCLUSIONS

In this work, a new Finite-Distinct macroelement model (M-DEM) is proposed that aims to combine the efficiency of simplified numerical modeling methods with the possibility of simulating OOP failure mechanisms. In the proposed M-DEM model, a given URM member is idealized as an assembly of deformable Finite Element (FE) macro-blocks (which account for compressive damage) and zero-thickness interface springs (representing potential shear-tensile failure planes), whose layout is determined *a priori* as a function of the bond pattern. This simple yet effective modeling strategy preserves the ability to reproduce in-plane (IP) responses of large-scale URM systems in a reasonable timeframe demonstrated previously [40], while also enabling simulation of OOP behavior.

First, to investigate the effect of FE mesh refinement on the OOP bending behavior, a parametric study (in which various wall aspect ratios and boundary conditions were considered) was conducted, allowing the selection of an optimal degree of discretization of the FE macro-blocks, balancing computation time and accuracy. Further, an analytically-based procedure is proposed that allows to reduce the number of FE subdivisions and interface springs in the OOP direction (and hence analysis time) without significantly affecting numerical accuracy. To this end, new expressions for M-DEM parameters are presented that force the equivalence between an ideal continuous system (with an infinite number of springs) and the employed discrete system. Because a single set of interface spring values must be effective for both IP/OOP bending problems, an iterative error minimization procedure is proposed to define values that are suitable for simulating coupled problems. Comparisons between continuous and equivalent discrete models indicate that similar results can be obtained with the proposed methodology, while reducing the analysis time more than 200%.

A comprehensive validation process was then undertaken, including the simulation of six quasi-static airbag tests and two dynamic free-release tests for one-way bending URM panels. Four wall specimens quasi-static under two-way bending actions were also considered for validation. The selected tests included both clay bricks and concrete block walls, characterized by markedly different geometrical and mechanical properties and subjected to a variety of boundary conditions and vertical loads. The M-DEM procedure was found to be capable of reproducing several failure mechanisms, ranging from crushing-dominated responses to those governed by

damage of mortar joints. Satisfactory predictions of force-displacement curves were also obtained. The approach was also applied to simulate the biaxial OOP response of confined concrete block masonry walls, and a good agreement was found between experimental and numerical outcomes.

The proposed methodology lays the foundation for future simulation of IP/OOP interaction, with the ability to simulate cumulative damage. Because of the relatively low computational cost, the methodology also enables the possibility of directly simulating failure of full-scale structures and building aggregates under more realistic dynamic loading and boundary conditions, on which further developments are thus warranted.

7. ACKNOWLEDGMENTS

Dr. Michele Godio (RISE, Research Institutes of Sweden) and Dr. Antonio Maria D'Altri (University of Bologna, Italy) are gratefully acknowledged for their precious assistance in accessing experimental and numerical data used in this manuscript for comparison purposes. The first author also expresses his gratitude to Prof. Anjali Mehrotra (Delft University of Technology, The Netherlands) for the fruitful discussions on the influence on the number of springs on numerical performance of DEM-based rocking models, as well as for her support in deriving some of the analytical formulations presented herein. Finally, the authors would like to thank three anonymous Reviewers, whose precious comments undoubtedly contributed to significantly improve the overall quality of this manuscript.

8. REFERENCES

[1] Clementi F, Ferrante A, Giordano E, Dubois F, Lenci S. Damage assessment of ancient masonry churches stroked by the Central Italy earthquakes of 2016 by the non-smooth contact dynamics method. Bull Earthq Eng 2019:1–32. https://doi.org/10.1007/s10518-019-00613-4.

[2] Sorrentino L, Cattari S, da Porto F, Magenes G, Penna A. Seismic behaviour of ordinary masonry buildings during the 2016 central Italy earthquakes. Bull Earthq Eng 2018:1–25. https://doi.org/10.1007/s10518-018-0370-4.

[3] Tomassetti U, Correia AA, Candeias PX, Graziotti F, Campos Costa A. Two-way bending out-of-plane collapse of a full-scale URM building tested on a shake table. Bull Earthq Eng 2019;17:2165–98. https://doi.org/10.1007/s10518-018-0507-5.

[4] Solarino F, Oliveira D V., Giresini L. Wall-to-horizontal diaphragm connections in historical buildings: A state-of-the-art review. Eng Struct 2019;199:109559. https://doi.org/10.1016/j.engstruct.2019.109559.

[5] Penna A, Lagomarsino S, Galasco A. A nonlinear macroelement model for the seismic analysis of masonry buildings. Earthq Eng Struct Dyn 2014;43:159–79.

[6] Sangirardi M, Liberatore D, Addessi D. Equivalent Frame Modelling of Masonry Walls Based on Plasticity and Damage. Int J Archit Herit 2019;13:1098–109. https://doi.org/10.1080/15583058.2019.1645240.

[7] Kallioras S, Graziotti F, Penna A. Numerical assessment of the dynamic response of a URM terraced house exposed to induced seismicity. Bull Earthq Eng 2019;17:1521–52. https://doi.org/10.1007/s10518-018-0495-5.

[8] Vanin F, Penna A, Beyer K. Equivalent-Frame Modeling of Two Shaking Table Tests of Masonry Buildings Accounting for Their Out-Of-Plane Response. Front Built Environ 2020;6:42. https://doi.org/10.3389/fbuil.2020.00042.

[9] Berti M, Salvatori L, Orlando M, Spinelli P. Unreinforced masonry walls with irregular opening layouts: reliability of equivalent-frame modelling for seismic vulnerability assessment. Bull Earthq Eng 2017;15:1213–39. https://doi.org/10.1007/s10518-016-9985-5.

[10] Parisi F, Augenti N. Seismic capacity of irregular unreinforced masonry walls with openings. Earthq Eng Struct Dyn 2013;42:101–21. https://doi.org/10.1002/eqe.2195.

[11] D'Ayala D, Shi Y. Modeling masonry historic buildings by multi-body dynamics. Int J Archit Herit 2011;5:483–512. https://doi.org/10.1080/15583058.2011.557138.

[12] Costa AA, Penna A, Arêde A, Costa A. Simulation of masonry out-of-plane failure modes by multi-body dynamics. Earthq Eng Struct Dyn 2015;44:2529–49.

[13] Mehrotra A, DeJong MJ. A CAD-interfaced dynamics-based tool for analysis of masonry collapse mechanisms. Eng Struct 2018;172:833–49. https://doi.org/10.1016/j.engstruct.2018.06.053.

[14] D'Altri AM, Sarhosis V, Milani G, Rots J, Cattari S, Lagomarsino S, et al. Modeling Strategies for the Computational Analysis of Unreinforced Masonry Structures: Review and Classification. Arch Comput Methods Eng 2019. https://doi.org/10.1007/s11831-019-09351-x.

[15] Sorrentino L, D'Ayala D, de Felice G, Griffith MC, Lagomarsino S, Magenes G. Review of Out-of-Plane Seismic Assessment Techniques Applied To Existing Masonry Buildings. Int J Archit Herit 2017;11:2–21. https://doi.org/10.1080/15583058.2016.1237586.

[16] Lemos J V. Discrete element modeling of masonry structures. Int J Archit Herit 2007;1:190–213. https://doi.org/10.1080/15583050601176868.
[17] Malomo D, DeJong MJ, Penna A. Distinct element modelling of the in-plane cyclic response of URM walls subjected to shear-compression. Earthq Eng Struct Dyn 2019. https://doi.org/10.1002/eqe.3178.
[18] Casolo S. A numerical study on the cumulative out-of-plane damage to church masonry façades due to a sequence of strong ground motions. Earthq Eng Struct Dyn 2017;46:2717–37. https://doi.org/10.1002/eqe.2927.
[19] Kawai T. New discrete models and their application to seismic response analysis of structures. Nucl Eng Des 1978;48:207–29.
[20] Godio M, Beyer K. Evaluation of force-based and displacement-based out-of-plane seismic assessment methods for unreinforced masonry walls through refined model simulations. Earthq Eng Struct Dyn 2019;48:454–75. https://doi.org/10.1002/eqe.3144.
[21] Pulatsu B, Bretas EM, Lourenço PB. Discrete element modeling of masonry structures: Validation and application. Earthq Struct 2016;11:563–82. https://doi.org/10.12989/eas.2016.11.4.563.
[22] D'Altri AM, de Miranda S, Castellazzi G, Sarhosis V. A 3D detailed micro-model for the in-plane and out-of-plane numerical analysis of masonry panels. Comput Struct 2018;206:18–30. https://doi.org/10.1016/j.compstruc.2018.06.007.
[23] Malomo D, Pinho R, Penna A. Numerical modelling of the out-of-plane response of full-scale brick masonry prototypes subjected to incremental dynamic shake-table tests. Eng Struct 2020;209:110298. https://doi.org/10.1016/j.engstruct.2020.110298.
[24] Çaktı E, Saygılı Ö, Lemos J V., Oliveira CS. Discrete element modeling of a scaled masonry structure and its validation. Eng Struct 2016;126:224–36. https://doi.org/10.1016/j.engstruct.2016.07.044.
[25] Galvez F, Giaretton M, Abeling S, Ingham J, Dizhur D. Discrete Element modelling of a two-storey unreinforced masonry scaled model. 16th Eur. Conf. Earthq. Eng., Thessaloniki, Greece: 2018.
[26] Aref AJ, Dolatshahi KM. A three-dimensional cyclic meso-scale numerical procedure for simulation of unreinforced masonry structures. Comput Struct 2013;120:9–23. https://doi.org/10.1016/J.COMPSTRUC.2013.01.012.
[27] Saloustros S, Pelà L, Cervera M, Roca P. An Enhanced Finite Element Macro-Model for the Realistic Simulation of Localized Cracks in Masonry Structures: A Large-Scale Application. Int J Archit Herit 2018;12:432–47. https://doi.org/10.1080/15583058.2017.1323245.
[28] Petracca M, Pelà L, Rossi R, Zaghi S, Camata G, Spacone E. Micro-scale continuous and discrete numerical models for nonlinear analysis of masonry shear walls. Constr Build Mater 2017;149:296–314. https://doi.org/10.1016/j.conbuildmat.2017.05.130.
[29] Silva LC, Lourenço PB, Milani G. Derivation of the out-of-plane behaviour of masonry through homogenization strategies: Micro-scale level. Comput Struct 2018;209:30–43. https://doi.org/10.1016/J.COMPSTRUC.2018.08.013.
[30] Petracca M, Pelà L, Rossi R, Oller S, Camata G, Spacone E. Multiscale computational first order homogenization of thick shells for the analysis of out-of-plane loaded masonry walls. Comput Methods Appl Mech Eng 2017;315:273–301. https://doi.org/10.1016/j.cma.2016.10.046.
[31] Maccarini H, Vasconcelos G, Rodrigues H, Ortega J, Lourenço PB. Out-of-plane behavior of stone masonry walls: Experimental and numerical analysis. Constr Build Mater 2018;179:430–52. https://doi.org/10.1016/j.conbuildmat.2018.05.216.
[32] Abrams DP, AlShawa O, Lourenço PB, Sorrentino L. Out-of-Plane Seismic Response of Unreinforced Masonry Walls: Conceptual Discussion, Research Needs, and Modeling Issues. Int J Archit Herit 2017;11:22–30. https://doi.org/10.1080/15583058.2016.1238977.
[33] Yi T, Moon FL, Leon RT, Kahn LF. Analyses of a two-story unreinforced masonry building. J Struct Eng 2006;132:653–62. https://doi.org/10.1061/(ASCE)0733-9445(2006)132:5(653).
[34] Lemos J V., Campos Costa A. Simulation of Shake Table Tests on Out-of-Plane Masonry Buildings. Part (V): Discrete Element Approach. Int J Archit Herit 2017;11:117–24. https://doi.org/10.1080/15583058.2016.1237587.
[35] Gams M, Anžlin A, Kramar M. Simulation of Shake Table Tests on Out-of-Plane Masonry Buildings. Part (III): Two-Step FEM Approach. Int J Archit Herit 2016;11:1–9. https://doi.org/10.1080/15583058.2016.1237589.
[36] Pantò B, Cannizzaro F, Caliò I, Lourenço PB. Numerical and experimental validation of a 3D macro-model for the in-plane and out-of-plane behavior of unreinforced masonry walls. Int J Archit Herit 2017;11:946–64.
[37] de Felice G. Out-of-plane seismic capacity of masonry depending on wall section morphology. Int J Archit Herit 2011;5:466–82. https://doi.org/10.1080/15583058.2010.530339.
[38] Mojsilović N, Marti P. Strength of masonry subjected to combined actions. ACI Struct J 1997;94:633–42.

[39] Itasca Consulting Group Inc. 3DEC. Three Dimensional Distinct Element Code 2013.
[40] Malomo D, DeJong MJ. A Macro-Distinct Element Model (M-DEM) for simulating the in-plane cyclic behavior of URM structures. Eng Struct 2020;227:111428. https://doi.org/10.1016/j.engstruct.2020.111428.
[41] Beyer K, Dazio A. Quasi-static cyclic tests on masonry spandrels. Earthq Spectra 2012;28:907–29. https://doi.org/10.1193/1.4000063.
[42] Magenes G, Calvi GM. In-plane seismic response of brick masonry walls. Earthq Eng Struct Dyn 1997;26:1091–112. https://doi.org/10.1002/(SICI)1096-9845(199711)26:11<1091::AID-EQE693>3.0.CO;2-6.
[43] Magenes G, Kingsley GR, Calvi GM. Seismic Testing of a Full-Scale , Two-Story Masonry Building : Test Procedure and Measured Experimental Response Seismic Testing of a Full-Scale , Two-Story Masonry Building : Test Procedure and Measured Experimental Response. Cons Naz Delle Ric Grup Naz per La Dif Dai Terremoti - Rep 30 - Dep Struct Mech Univ Pavia [in Ital 1995. https://doi.org/10.13140/RG.2.1.4590.2962.
[44] Penner O, Elwood KJ. Out-of-plane dynamic stability of unreinforced masonry walls in one-way bending: Shake table testing. Earthq Spectra 2016;32:1675–97. https://doi.org/10.1193/011415EQS009M.
[45] Griffith MC, Vaculik J, Lam NTK, Wilson J, Lumantarna E. Cyclic testing of unreinforced masonry walls in two-way bending. Earthq Eng Struct Dyn 2007;36:801–21. https://doi.org/10.1002/eqe.654.
[46] Beyer K. Peak and residual strengths of brick masonry spandrels. Eng Struct 2012;41:533–47. https://doi.org/10.1016/j.engstruct.2012.03.015.
[47] Sharma S, Graziotti F, Magenes G. Torsional shear strength of unreinforced brick masonry bed joints. Constr Build Mater 2021;275:122053. https://doi.org/10.1016/j.conbuildmat.2020.122053.
[48] Malomo D, Pinho R, Penna A. Numerical modelling of the out-of-plane response of full-scale brick masonry prototypes subjected to incremental dynamic shake-table tests. Eng Struct 2020;209. https://doi.org/10.1016/j.engstruct.2020.110298.
[49] Feenstra PH, De Borst R. A composite plasticity model for concrete. Int J Solids Struct 1996;33:707–30. https://doi.org/10.1016/0020-7683(95)00060-N.
[50] Marti J, Cundall P. Mixed discretization procedure for accurate modelling of plastic collapse. Int J Numer Anal Methods Geomech 1982;6:129–39. https://doi.org/10.1002/nag.1610060109.
[51] Zucchini A, Lourenço PB. A micro-mechanical model for the homogenisation of masonry. Int J Solids Struct 2002;39:3233–55. https://doi.org/10.1016/S0020-7683(02)00230-5.
[52] Drougkas A, Roca P, Molins C. Numerical prediction of the behavior, strength and elasticity of masonry in compression. Eng Struct 2015;90:15–28. https://doi.org/10.1016/j.engstruct.2015.02.011.
[53] Pandey BH, Meguro K. Simulation of Brick masonry wall behavior under in plane lateral loading using applied element method. 13th World Conf. Earthq. Eng. Vancouver, BC, Canada, August, vol. 16, 2004.
[54] Lourenco P, Rots J, Blaauwendraad J. Continuum Model for Masonry: Parameter Estimation and Validation. J Struct Eng 1998;124:642–52. https://doi.org/10.1061/(ASCE)0733-9445(1998)124:6(642).
[55] Cundall PA. Formulation of a three-dimensional distinct element model-Part I. A scheme to detect and represent contacts in a system composed of many polyhedral blocks. Int J Rock Mech Min Sci 1988. https://doi.org/10.1016/0148-9062(88)92293-0.
[56] Godio M, Beyer K. Analytical model for the out-of-plane response of vertically spanning unreinforced masonry walls. Earthq Eng Struct Dyn 2017;46:2757–76. https://doi.org/10.1002/eqe.2929.
[57] Shawa O Al, de Felice G, Mauro A, Sorrentino L. Out-of-plane seismic behaviour of rocking masonry walls. Earthq Eng Struct Dyn 2012;41:949–68. https://doi.org/10.1002/eqe.1168.
[58] Michalewicz Z, Janikow CZ. Genetic algorithms for numerical optimization. Stat Comput 1991;1:75–91. https://doi.org/10.1007/BF01889983.
[59] Graziotti F, Tomassetti U, Sharma S, Grottoli L, Magenes G. Experimental response of URM single leaf and cavity walls in out-of-plane two-way bending generated by seismic excitation. Constr Build Mater 2019;195:650–70. https://doi.org/10.1016/j.conbuildmat.2018.10.076.
[60] Yokel FY, Mathey RG, Dikkers RD. Strength of masonry walls under compressive and transverse loads. Dep Commer United States, Natl Bur Stand 1971;34.
[61] Derakhshan H, Griffith MC, Ingham JM. Airbag testing of multi-leaf unreinforced masonry walls subjected to one-way bending. Eng Struct 2013;57:512–22. https://doi.org/10.1016/j.engstruct.2013.10.006.
[62] Doherty K, Griffith MC, Lam N, Wilson J. Displacement-based seismic analysis for out-of-plane bending of unreinforced masonry walls. Earthq Eng Struct Dyn 2002;31:833–50. https://doi.org/10.1002/eqe.126.
[63] Chee Liang N. Experimental And theoretical investigation of the behaviour of brickwork cladding panel subjected to lateral loading. PhD Diss Dep Civ Environ Eng Univ Edinburgh 1996.

[64] Drysdale RG, Essawy AS. Out-of-plane bending of concrete block walls. J Struct Eng (United States) 1988;114:121–33. https://doi.org/10.1061/(ASCE)0733-9445(1988)114:1(121).
[65] Macorini L, Izzuddin BA. A non-linear interface element for 3D mesoscale analysis of brick-masonry structures. Int J Numer Methods Eng 2011;85:1584–608. https://doi.org/10.1002/nme.3046.
[66] Varela-Rivera JL, Navarrete-Macias D, Fernandez-Baqueiro LE, Moreno EI. Out-of-plane behaviour of confined masonry walls. Eng Struct 2011;33:1734–41. https://doi.org/10.1016/j.engstruct.2011.02.012.
[67] Varela-Rivera J, Moreno-Herrera J, Lopez-Gutierrez I, Fernandez-Baqueiro L. Out-of-plane strength of confined masonry walls. J Struct Eng (United States) 2012;138:1331–41. https://doi.org/10.1061/(ASCE)ST.1943-541X.0000578.